IEEE Photonics Journal
An IEEE Photonics Society Publication

Open Access

Quadratic Soliton Combs in Doubly Resonant Dispersive Optical Parametric Oscillators

Volume 12, Number 2, April 2020

Aiguo Sheng
Chaoxiang Xi
Zhenyu Yang
Xiaoshun Jiang
Guangqiang He

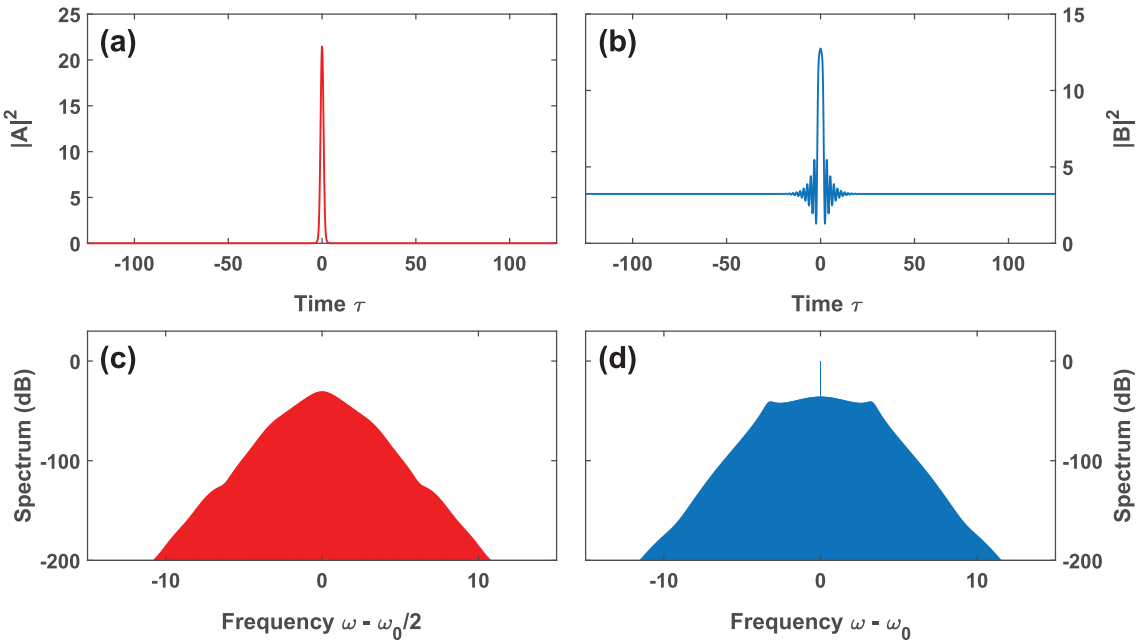

DOI: 10.1109/JPHOT.2020.2966533

Quadratic Soliton Combs in Doubly Resonant Dispersive Optical Parametric Oscillators

Aiguo Sheng,[1] **Chaoxiang Xi**,[1] **Zhenyu Yang**,[2] **Xiaoshun Jiang**,[3] **and Guangqiang He** [1]

[1]State Key Laboratory of Advanced Optical Communication Systems and Networks, Department of Electronic Engineering, Shanghai Jiao Tong University, Shanghai 200240, China
[2]Wuhan National Laboratory for Optoelectronics, School of Optical and Electronic Information, Huazhong University of Science and Technology, Wuhan 430074, China
[3]National Laboratory of Solid State Microstructures, College of Engineering and Applied Sciences and School of Physics, Nanjing University, Nanjing 210093, China

DOI:10.1109/JPHOT.2020.2966533

Manuscript received November 19, 2019; revised January 10, 2020; accepted January 10, 2020. Date of publication January 13, 2020; date of current version March 9, 2020. This work was supported in part by the National Natural Science Foundation of China (NSFC) under Grants 61475099 and 11574144, and in part by the Key R&D Program of Guangdong Province under Grant 2018B030325002. Corresponding author: Guangqiang He (e-mail: gqhe@sjtu.edu.cn).

Abstract: We present temporal quadratic solitons in doubly resonant temporal dispersive optical parametric oscillators without a walk-off in numerical simulations. In frequency domain, these cavity solitons correspond to coherent dual-combs with smooth envelopes in half-harmonic and pump fields. We also investigate the soliton existence region, and the soliton behavior with parameters in this cavity system. We believe our work offers valuable insights into the practical generation of quadratic soliton combs in optical parametric oscillators.

Index Terms: Quadratic solitons, frequency combs, optical parametric oscillators.

1. Introduction

Optical frequency combs (OFCs) based on Kerr cavities have led to tremendous research interests in the past decade [1], [2]. Recently, OFCs due to the quadratic nonlinearity also have been proposed [3], [4]. Compared with Kerr frequency combs, OFCs can be generated by quadratic cavities with a low driving threshold in both the pump field and the field that is separate from the pump frequency, where suitable pump sources are difficult to obtain [5], [6]. As an example, the near-infrared pump may create visible frequency combs by second-harmonic generation (SHG), which is useful in optical atomic clock and astronomical calibration applications [7], [8]. What's more, half-harmonic generation (HHG) in optical parametric oscillators (OPOs) is capable of the formation of mid-infrared combs, providing efficient photonic solutions for molecular sensing and non-classical computing [9]–[11].

Quadratic combs through the locking of domain walls in doubly resonant dispersive OPOs have been recently studied [12]. As reported in Kerr frequency combs, to unlock the full potential of OFCs, cavity solitons (CSs) are the most important and desirable waveforms [13]–[17]. Cavity

solitons correspond to a periodic train of coherent, mode-locked, and ultrashort pulses in temporal domain, representing the ultralow-noise OFCs with smooth envelopes in frequency domain, which are revolutionary in many applications. Recently, soliton frequency combs in OPOs with the presence of both quadratic and cubic nonlinearities have been theoretically reported [18], [19].

In this work, we study the existence of temporal solitons in the dispersive OPO cavity system with the pure quadratic nonlinearity, for which both the half-harmonic field centered at frequency $\omega_0/2$ and the pump field centered at frequency ω_0 are resonant. We consider the cavity configuration that eliminates the temporal walk-off between the half-harmonic field and the pump field, since the walk-off is detrimental for the formation of pulse-like localized solutions in quadratic cavities [6], [12]. We also investigate the effect of the pump strength, the laser frequency detuning, and the dispersion on the solitons.

2. Simulation Model

As introduced in Ref. [12], the doubly resonant phase-matched degenerate OPO system can be described by two coupled mean-field equations, in the normalized form:

$$\frac{\partial A}{\partial t} = \left[-(1 + i\Delta_1) - i\beta_1 \frac{\partial^2}{\partial \tau^2} \right] A + iBA^*, \tag{1}$$

$$\frac{\partial B}{\partial t} = \left[-(\alpha + i\Delta_2) - d\frac{\partial}{\partial \tau} - i\beta_2 \frac{\partial^2}{\partial \tau^2} \right] B + iA^2 + S, \tag{2}$$

where A is the slowly varying envolope of the half-harmonic field centered at frequency $\omega_0/2$ and B is the slowly varying envolope of the pump field centered at frequency ω_0. t is the slow-time variable, τ is the fast-time variable, α is the ratio of the loss of the pump field to the loss of the half-harmonic field, $\Delta_{1,2}$ are detunings of the cavity, d is the temporal walk-off, $\beta_1 = \mathrm{sgn}[k_1^{''}]$ and $\beta_2 = k_2^{''}/|k_1^{''}|$ represent group velocity dispersion (GVD) parameters ($k_{1,2}^{''}$ are GVD coefficients at $\omega_0/2$ and ω_0, respectively), and S is the strength of the continuous-wave (CW) pump. It is noteworthy that this model is formally equivalent to the equations describing one-dimensional spatial diffractive OPOs [20], [21]. In this model, the diffraction parameters are replaced by the GVD parameters and the spatial dimension is changed into temporal dimension. Here, we consider the practical OPO cavity system without a walk-off and use the parameters in Ref. [6], so that $\alpha = 1$, $d = 0$, $\beta_1 = -1$, $\beta_2 = 0.5$, and $\Delta_2 = 2\Delta_1$. This OPO cavity system can be realized by using a quasi-phase-matched $LiNbO_3$ crystal, and the centered wavelengths of the half-harmonic and pump fields in this system are 2707 nm and 1354 nm, respectively, which is the inverse of the SHG cavity system in Ref. [6].

3. Numerical Simulation Results

Equations 1 and 2 can be numerically propagated over the slow-time variable t with a split-step Fourier method, where the periodic boundary of the fast-time variable τ is $[-\tau_s/2, \tau_s/2]$ (τ_s is the normalized round-trip time, so that the normalized free spectral range (FSR) τ_s^{-1} represents the spacing of the normalized Fourier frequency grid in the simulation). To numerically find the soliton solutions, we use a Gaussian pulse with the complex amplitude $A_{\mathrm{in}}(\tau) = (A_{\mathrm{real}} + iA_{\mathrm{imag}})\exp(-(\tau/\tau_{\mathrm{in}})^2)$ in the half-harmonic (A) field and small noise in the pump (B) field as the initial seeds to excite localized solutions in the parameter plane of Δ_1 and S. The final localized steady-state solutions can be obtained from the evolution of the initial waveforms. We also verify the stability of the solutions over a sufficiently long simulation ($t = 20000$). In our simulations, the number of frequency modes for each field is 2048 and the normalized round-trip time τ_s is 250. The parameters of the initial input pulse are $A_{\mathrm{real}} = A_{\mathrm{imag}} = 5$ and $\tau_{\mathrm{in}} = 5$.

Figure 1 shows an example of the CSs. As shown in Figs. 1(a) and 1(b), both the half-harmonic and pump fields display a localized ultrashort pulse in the center of the fast-time window. The soliton in A field has no CW pedestal, while the soliton in B field displays a peak with damped oscillations on both sides in a CW background. The corresponding spectra of the solitons in Figs. 1(a) and

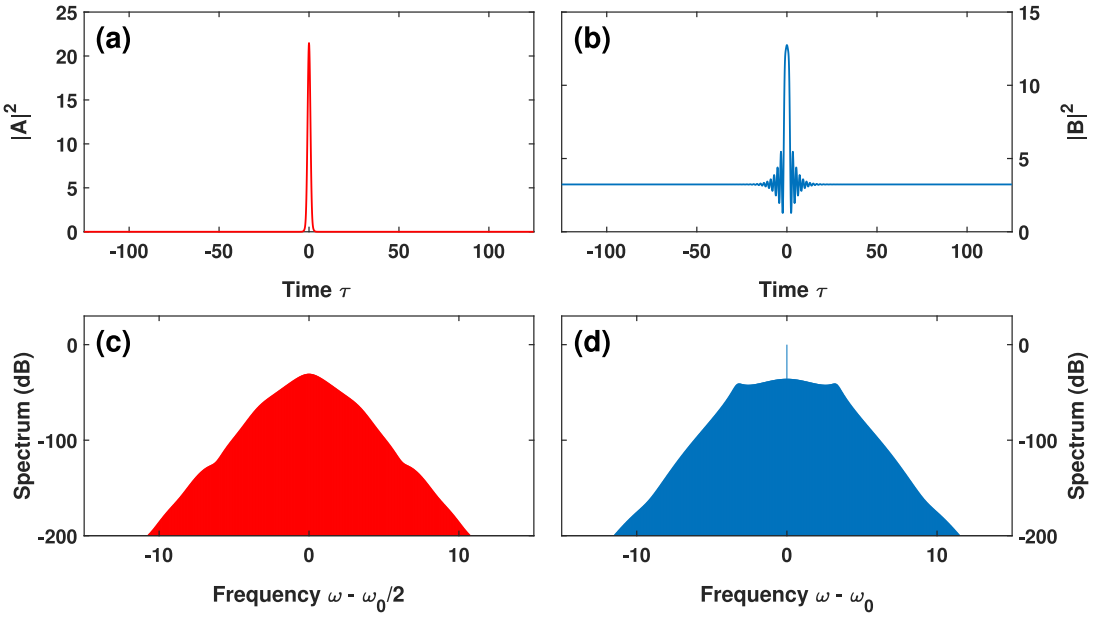

Fig. 1. Normalized intracavity power (top) and spectra (bottom) of a CS in the half-harmonic field (red) and the pump field (blue) and spectra for $\Delta_1 = 2.74$ and pump strength $S = 10.0$, where $\beta_1 = -1$ and $\beta_2 = 0.5$.

1(b) are shown in 1(c) and 1(d), respectively. Either spectrum's envelope is smooth, so that the frequency modes in a certain band have similar intensities, which is important for the mid-infrared spectroscopic sensing and massively parallel coherent optical communications [22], [23]. For a given set of parameters, the amplitude and width of the CSs are unique, which is same as the CSs in the SHG cavity system [6].

Since the localized structures with different polarities in the half-harmonic field are both the solutions of this OPO cavity system [12], it is natural to investigate the polarity of the CSs obtained here. We also find that the CSs with the opposite polarities in the half-harmonic field can exist in the same parameter region, as shown in Figs. 2(a) and 2(b). The CS with the opposite polarity in Fig. 2(b) is excited by using the initial pulse above with opposite amplitude in the same parameter region. Unlike the CSs in A field, CSs in B field only have one polarity. The corresponding CSs in B field of the opposite CSs in Figs. 2(a) and 2(b) have the same complex amplitude, which is shown in Fig. 2(c). This can be easily understood that Eq. 1 is linear for A, while Eq. 2 with the term of iA^2 and S is nonlinear for B, so that if $A_{\text{sol}}(t, \tau)$ is a localized solution of Eqs. 1 and 2, $-A_{\text{sol}}(t, \tau)$ is also a satisfied solution, but this is not true for $B_{\text{sol}}(t, \tau)$. Also, due to the square term (iA^2) in Eq. 2, $A_{\text{sol}}(t, \tau)$ and $-A_{\text{sol}}(t, \tau)$ have the same effect on Eq. 2, resulting in only one polarity and the same complex amplitude for the corresponding localized solutions in B field.

Figure 3 shows the soliton existence region in the (Δ_1, S)-parameter plane. The locations of a number of the soliton solutions are marked by the dark red points, and these points outline the grey area, which indicates the soliton existence region. As shown in Fig. 3, the soliton existence region is located in a thin band, and becomes farther from the resonance and wider with the pump strength increasing. For $S = 17$, the detuning range length of the soliton existence region for Δ_1 is about 0.36. According to the normalization in Ref. [12], the CW pump is $B_{in} = S\alpha_1^2/(\sqrt{\theta_2}\kappa L)$, the detuning is $\delta_{1,2} = \Delta_{1,2}\alpha_1/t_r$, and the round-trip time is $t_r = \tau_s/\sqrt{2\alpha_1/(|k_1''|L)}$, where α_1 is the cavity loss in the half-harmonic field, θ_2 is the power transmission coefficient at ω_0, and κ is the nonlinear coefficient. Assuming the critical coupling $\theta_2 = \alpha_1$, the cavity finesse $F = \pi/\alpha_1 = 160$, the nonlinear coefficient $\kappa = 11.14$ W$^{-1/2}$/m, the crystal length $L = 15$ mm, and the GVD coefficient $k_1'' \approx -0.32$ ps^2/m at $\omega_0/2$ [6], the system has a soliton existence range of 26 MHz in pump frequency detuning with a pump power of 78 mW and a round-trip time of 87 ps.

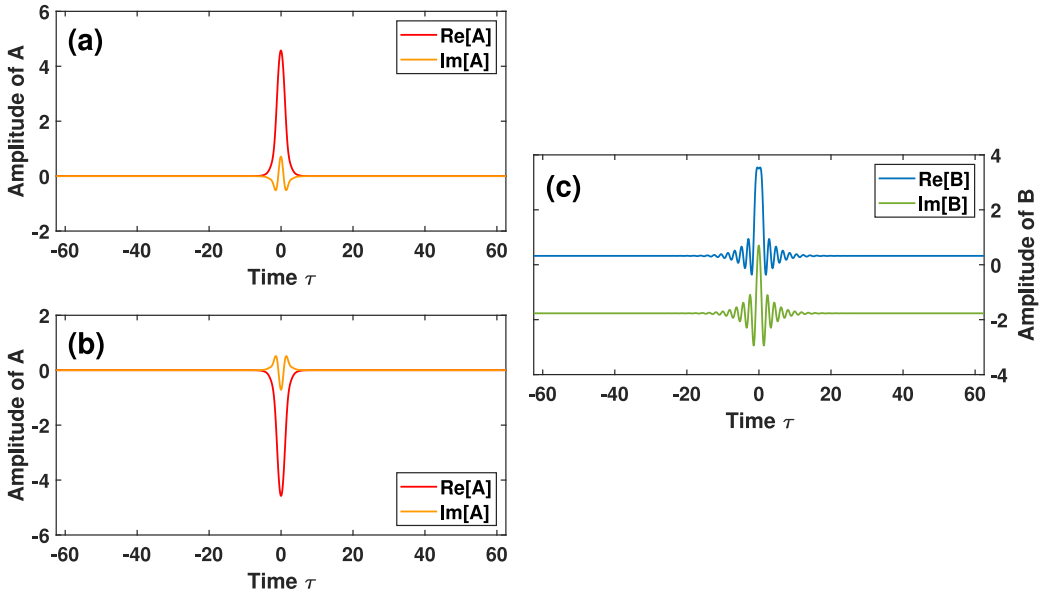

Fig. 2. Complex amplitude of the solitons with (a) the positive polarity and (b) the negative polarity in Fig. 1(a). (c) The corresponding solitons in *B* field of the solitons in (a) and (b) have the same complex amplitude.

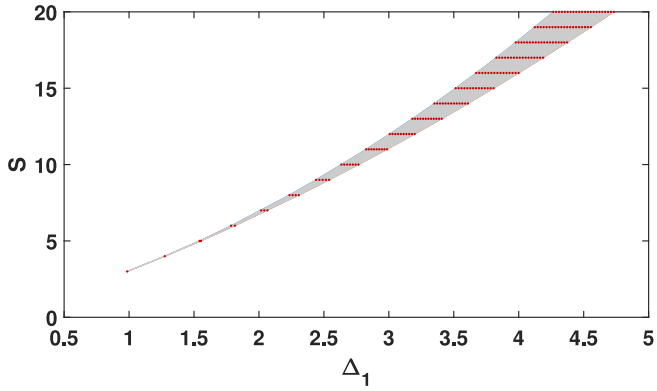

Fig. 3. (Δ_1, S)-parameter plane for the solutions of Eqs. 1 and 2. The dark red points show the locations of the soliton solutions and the grey area indicates the soliton existence region.

Next, we investigate the influence of the simulation parameters on the pulse width and the peak intensity of CSs. Firstly, we choose six typical points in the (Δ_1, S)-parameter plane in Fig. 3, as shown in Fig. 4(a), where points 1–6 represent (Δ_1, S) = (3.84,17.0), (4.16,17.0), (4.00,16.2), (4.00,17.8), (2.74,10.0), and (4.00,17.0), respectively. Here, the route from point i to point j is writen as ($i-j$). We consider the evolution of the soliton profile along the three routes (1–2, 3–4, and 5–6). S is fixed to 17.0 for the route (1–2) (yellow dashed line) and Δ_1 is fixed to 4.00 for the route (3–4) (green dashed line). For the route (5–6) (orange dashed line), both Δ_1 and S increase along the band of the existence region. We choose the sample points uniformly along these routes, which are shown in Figs. 4(b)–(d). For exhibiting the profile changes of the CSs in detail, we capture the waveforms in the fast-time window $\tau \in [-5,5]$. Fig. 4(b) shows the evolution of the soliton waveforms along the route (1–2) in *A* (top) and *B* (bottom) fields. The increase of the detuning Δ_1 mainly induces the decrease of the pulse width both in *A* and *B* fields, and the center of *B* field is seen to exhibit the process from a small hollow to a bump. The evolution of

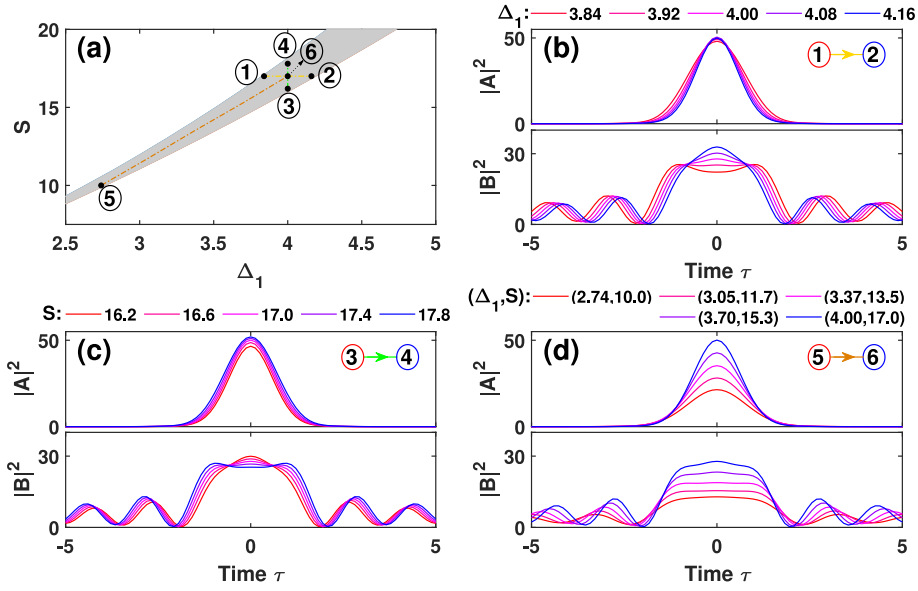

Fig. 4. (a) The soliton existence region in the (Δ_1, S)-parameter plane. Points 1-6 represent (Δ_1, S) = (3.84,17.0), (4.16,17.0), (4.00,16.2), (4.00,17.8), (2.74,10.0), and (4.00,17.0), respectively. (b), (c), and (d) show the evolution of the soliton waveforms in A and B fields along routes (1–2), (3–4), and (5–6), respectively.

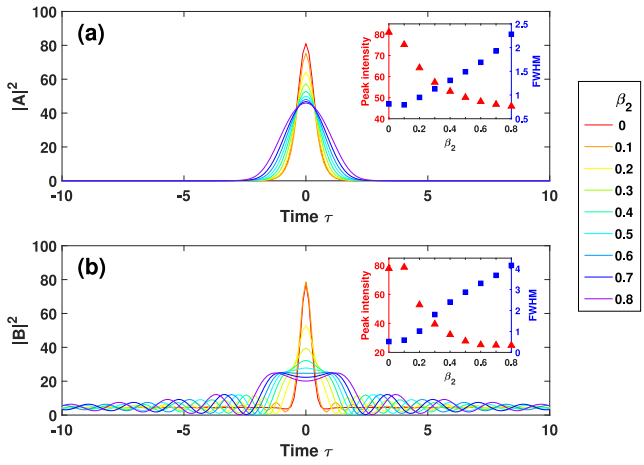

Fig. 5. Influence of the magnitude of the dispersion parameter β_2 on (a) A and (b) B fields. Here, $\beta_1 = -1$, $\Delta_1 = 4.00$, and $S = 17.0$. Insets: the dependence of the full width at half maxima (FWHM) and peak intensity of the solitons with β_2.

the soliton waveforms along the route (3–4) is shown in Fig. 4(c). The effect of the increase in the pump strength S induces both the broadening of the pulses and the increase of the soliton intensity in general (except the center of B field, where the bump becomes a small hollow gradually). Last, we consider the effect of the increase in both Δ_1 and S, as shown in Fig. 4(d). Obviously, along the route (5–6), the pulse peaks of the CSs in both A and B fields are greatly increased. The CSs in point 6 have nearly twice the peak intensity of the CSs in point 5. The pulse width of the CSs (neglecting the damped oscillations) changes slightly, which may be explained that the opposite effects on the pulse width induced by Δ_1 and S cancel each other out to a certain degree.

Finally, we consider the effect of the GVD coefficients. It is worth mentioning that the sign of the GVD coefficient is an important factor for the soliton existence and other properties. An analysis

of the sign of the two GVD coefficients is beyond present scope and subject of our future work. Here, since the GVD coefficient β_1 is normalized to a unit value and β_2 is normalized by the value of β_1, we investigate the effect of GVD by using different values of β_2 in simulations. It is found that the soliton existence region is influenced by the GVD. For simplicity, we keep the sign of β_1 and β_2, and only choose the β_2 for which we can still obtain the stable soliton solutions at the point $(\Delta_1, S) = (4.00,17.0)$. As shown in Fig. 5, the effect of reducing β_2 is essentially to decrease the pulse width of the CSs and enhance the peak intensity in both *A* and *B* fields (the insets show the dependence of the pulse width and peak intensity with β_2). It is worth noting that when β_2 becomes small enough, the damped oscillations in *B* field tends to decrease. Especially, we investigate the soliton solution for $\beta_2 = 0$ (red line). In this case, it is interesting that the CS in *B* field exhibit no damped oscillations on both sides, as shown in Fig. 5(b).

4. Conclusions

We have presented the generation of quadratic soliton combs in the doubly resonant OPO cavity system with a practical configuration in the absence of temporal walk-off. The soliton existence region in this cavity system is numerically investigated. We also have investigated the influence of the frequency detuning, the pump strength, and the dispersion parameters on the solitons. We expect that our work will have a significant predictive impact on the generation of soliton combs in OPO cavities and contribute to some advanced fields in future [24], [25].

Note: When the original version of this paper was under review, the authors became aware of a recently published work by Pedro Parra-Rivas *et al.* on a similar topic [26]. The soliton presented here is actually a particular type of the localized structures studied in Ref. [26], which are formed by the locking of domain walls between two CW states. The differences between these solutions shown in Ref. [26] and this paper (such as the opposite polarity in *B* field, the opposite detuning position, and the swap between the real and imaginary amplitude) are due to the opposite sign of the GVD parameter in *A* field (β_1) used.

Acknowledgment

The authors thank the anonymous reviewers for their valuable comments.

References

[1] P. Del'Haye, A. Schliesser, O. Arcizet, T. Wilken, R. Holzwarth, and T. J. Kippenberg, "Optical frequency comb generation from a monolithic microresonator," *Nature*, vol. 450, no. 7173, pp. 1214–1217, 2007.
[2] T. J. Kippenberg, R. Holzwarth, and S. A. Diddams, "Microresonator-based optical frequency combs," *Science*, vol. 332, no. 6029, pp. 555–559, 2011.
[3] F. Leo *et al.*, "Walk-off-induced modulation instability, temporal pattern formation, and frequency comb generation in cavity-enhanced second-harmonic generation," *Phys. Rev. Lett.*, vol. 116, no. 3, 2016, Art. no. 033901.
[4] S. Mosca *et al.*, "Modulation instability induced frequency comb generation in a continuously pumped optical parametric oscillator," *Phys. Rev. Lett.*, vol. 121, no. 9, 2018, Art no. 093903.
[5] T. Hansson *et al.*, "Singly resonant second-harmonic-generation frequency combs," *Phys. Rev. A*, vol. 95, no. 1, 2017, Art. no. 013805.
[6] T. Hansson, P. Parra-Rivas, M. Bernard, F. Leo, L. Gelens, and S. Wabnitz, "Quadratic soliton combs in doubly resonant second-harmonic generation," *Opt. Lett.*, vol. 43, no. 24, pp. 6033–6036, 2018.
[7] J. Ma *et al.*, "Visible Kerr comb generation in a high-q silica microdisk resonator with a large wedge angle," *Photon. Res.*, vol. 7, no. 5, pp. 573–578, 2019.
[8] S. Miller, K. Luke, Y. Okawachi, J. Cardenas, A. L. Gaeta, and M. Lipson, "On-chip frequency comb generation at visible wavelengths via simultaneous second- and third-order optical nonlinearities," *Opt. Express*, vol. 22, no. 22, pp. 26 517–26 525, 2014.
[9] A. Marandi, "Half-harmonic generation: Enabling photonic solutions for molecular sensing and non-classical computing," in *Nonlinear Optics*. Optical Society of America, 2019, pp. NM1A–3.
[10] C. Y. Wang *et al.*, "Mid-infrared optical frequency combs at 2.5 μm based on crystalline microresonators," *Nature Commun.*, vol. 4, pp. 1345–1351, 2013.
[11] P. L. McMahon *et al.*, "A fully programmable 100-spin coherent ising machine with all-to-all connections," *Science*, vol. 354, no. 6312, pp. 614–617, 2016.

[12] P. Parra-Rivas, L. Gelens, T. Hansson, S. Wabnitz, and F. Leo, "Frequency comb generation through the locking of domain walls in doubly resonant dispersive optical parametric oscillators," *Opt. Lett.*, vol. 44, no. 8, pp. 2004–2007, 2019.
[13] F. Ferdous *et al.*, "Spectral line-by-line pulse shaping of on-chip microresonator frequency combs," *Nature Photon.*, vol. 5, no. 12, pp. 770–776, 2011.
[14] T. Herr *et al.*, "Universal formation dynamics and noise of Kerr-frequency combs in microresonators," *Nature Photon.*, vol. 6, no. 7, pp. 480–487, 2012.
[15] T. Herr *et al.*, "Temporal solitons in optical microresonators," *Nature Photon.*, vol. 8, no. 2, pp. 145–152, 2014.
[16] H. Guo *et al.*, "Universal dynamics and deterministic switching of dissipative Kerr solitons in optical microresonators," *Nature Phys.*, vol. 13, no. 1, pp. 94–102, 2017.
[17] T. J. Kippenberg, A. L. Gaeta, M. Lipson, and M. L. Gorodetsky, "Dissipative Kerr solitons in optical microresonators," *Science*, vol. 361, no. 6402, 2018, Art. no. eaan8083.
[18] T. Hansson *et al.*, "Single envelope equation modeling of multi-octave comb arrays in microresonators with quadratic and cubic nonlinearities," *J. Opt. Soc. Amer. B*, vol. 33, no. 6, pp. 1207–1215, 2016.
[19] A. Villois, N. Kondratiev, I. Breunig, D. N. Puzyrev, and D. V. Skryabin, "Frequency combs in a microring optical parametric oscillator," *Opt. Lett.*, vol. 44, no. 18, pp. 4443–4446, 2019.
[20] S. Longhi, "Localized structures in optical parametric oscillation," *Physica Scripta*, vol. 56, no. 6, pp. 611–618, 1997.
[21] K. Staliunas and V. J. Sánchez-Morcillo, "Localized structures in degenerate optical parametric oscillators," *Opt. Commun.*, vol. 139, no. 4-6, pp. 306–312, 1997.
[22] N. Picqué and T. W. Hänsch, "Mid-IR spectroscopic sensing," *Opt. Photon. News*, vol. 30, no. 6, pp. 26–33, 2019.
[23] P. Marin-Palomo *et al.*, "Microresonator-based solitons for massively parallel coherent optical communications," *Nature*, vol. 546, no. 7657, pp. 274–279, 2017.
[24] J. Roslund, R. M. De Araujo, S. Jiang, C. Fabre, and N. Treps, "Wavelength-multiplexed quantum networks with ultrafast frequency combs," *Nature Photon.*, vol. 8, no. 2, pp. 109–112, 2014.
[25] N. C. Menicucci, S. T. Flammia, and O. Pfister, "One-way quantum computing in the optical frequency comb," *Phys. Rev. Lett.*, vol. 101, no. 13, 2008, Art. no. 130501.
[26] P. Parra-Rivas, L. Gelens, and F. Leo, "Localized structures in dispersive and doubly resonant optical parametric oscillators," *Phys. Rev. E*, vol. 100, no. 3, 2019, Art. no. 032219.